Drying of mortar at ambient temperature studied using high resolution neutron tomography and numerical modeling

Hani Cheikh Sleiman, Alessandro Tengattini, Matthieu Briffaut, Bruno Huet, Stefano Dal Pont

Drying of mortar at ambient temperature studied using high resolution neutron tomography and numerical modelling

Hani Cheikh Sleiman[a,b,*], Alessandro Tengattini[a,c], Matthieu Briffaut[a,e], Bruno Huet[d], Stefano Dal Pont[a]

[a] *University Grenoble Alpes, CNRS, Grenoble INP, 3SR, 38000.*
[b] *Department of Mechanical Engineering, University College London, London, UK.*
[c] *Institute Laue-Langevin, 71 avenue des Martyrs - CS 20156, 38042 Grenoble Cedex 9, France.*
[d] *LafargeHolcim Reasearch center, Saint-Quentin-Fallavier, France.*
[e] *Laboratoire de Mécanique, Multiphysique, Multiéchelle (LaMcube) FRE CNRS 2016, 59655, Villeneuve d'Ascq Cedex, France*

Abstract

The drying of cement-based materials, naturally occurring in most civil engineering contexts, affects their thermal, hydraulic and mechanical properties and is a leading contributor to the loss of their durability potential. The techniques conventionally employed to study this moisture transfer, such as gravimetry weight loss and point-wise sensor-based measurements, are often destructive and cannot characterise the local driving phenomena in 4D (3D+time), essential given the highly heterogeneous nature of the involved processes. Conversely, full-field techniques, and notably neutron tomography, are non-invasive and ideal for measuring the moisture transport process due to the high attenuation of neutron by hydrogen.

In this study, the moisture distribution of a set of cylindrical mortar samples was characterised at different hydric states, as imposed through drying in a thermo-hydrically controlled environment (T=20 °C, RH=35 %). The lateral surfaces of the samples were sealed to impose a unidirectional moisture flow. The main phases of the mortar (aggregates, cement paste and voids), visible at the 30μm resolution adopted, were separated, and saturation profiles were deduced and validated against the mortar mixture ratios and weight loss measurements.

Besides the intrinsic interest of the spatio-temporal evolution of the local extracted saturation, these hydric gradients are essential to calibrate numerical models, as the commonly used Finite Element model presented here. A minimisation algorithm was developed for this purpose to automate, optimise and ensure a more objective numerical-experimental calibration procedure. This has allowed the identification of key hydric parameters such as the convective exchange coefficient and the intrinsic permeability.

*Corresponding author
Email address: hani.cheikh.sleiman@outlook.com (Hani Cheikh Sleiman)

1. Introduction

The naturally occurring drying of cement-based materials has inevitable and significant effects on their durability. After casting, cement-based materials generally have a higher hygrometry than the surrounding environment. The water located in the porous network tends then to migrate towards the external environment to establish hydric equilibrium. This water loss induces drying shrinkage which gets restrained not only by the presence of aggregates, but also by the the core of the sample which remains saturated for a longer time. These differential deformations generate high stresses that can lead to cracking.

Additionally, the evolution of the relative humidity in the interconnected pores affects the hydraulic properties of the material, such as hydraulic conductivity and diffusivity [1][2]), chemical properties (such as hydration degree [3] and the kinetics of degrading chemical reactions [4]), thermal properties (such as thermal conductivity [5]), mechanical properties (such as creep [6]), fire resistance [7][8], *etc.* It follows that characterising the hydric state and its evolution is pivotal for understanding its implications on the structural integrity of cement-based materials.

Several methods have been adopted in the literature to characterize the cement based material hydric state and properties. They can be broadly classified in three main categories: bulk-averaged or point-wise methods, full-field measurement techniques and indirect numerical modeling methods. Within the first group, the measure of the evolution of mass loss along time of a sample subject to drying is perhaps the most adopted method [9][10]. Despite its widespread adoption, perhaps related to the ease of its implementation, this measurement is a macroscopic average of the highly heterogeneous response of the materials and cannot provide insight about the spatial distribution of water content. To overcome this limitation, several authors have employed sensor-based measurement tools to assess relative humidity in a particular point in space [11][12]. However, these point-wise approaches are usually invasive and might show variable measurements depending on their proximity to different species (porosity, aggregates) in a heterogeneous porous medium such as concrete. Furthermore, they require the identification of the sorption/desorption isotherms of the material to relate the relative humidity to saturation [13].

In the last few decades, the development of full-field measurement techniques have allowed unprecedented insight into local processes [14][15]. When studying moisture transfer in porous media, multiple full-field techniques have been explored, such as Nuclear Magnetic Resonance NMR [16] [17][18], Radiation attenuation techniques (such as Gammadensimetry [19]), Electrical techniques (Electrical Capacitance Tomography ECT [20]) and Electromagnetic Non-Destructive Evaluation ENDE techniques [21].

A particularly effective tool is Neutron Imaging, which lend itself as a very powerful non-destructive and non-invasive technique to study the moisture distribution in porous materials due to the high attenuation of neutrons by hydrogen [22][23][24]. The 2D/3D attenuation fields resulting from the radiography/tomography can be correlated to water content after due calibration [25][26].

Beside the intrinsic interest of understanding the evolving moisture profiles, the spatial distribution of moisture content is essential to rigorously calibrate thermo-hydric numerical models [27] [28]. This numerical calibration can, in turn, be used to characterize the hydraulic properties of the material which are anomalously characterized experimentally, such as the intrinsic permeability. In fact, the experimental measurement of this property shows a high sensitivity to the used fluid. The gas permeability can be up to three orders of magnitude higher than water permeability both because of pre-drying induced cracking and pore-wall physically adsorbed water removal. On the other hand, the water permeability can only be measured in saturated conditions, thus in a configuration where drying cracks effect on the drying kinetics are not taken into account. For these reasons, it is generally agreed that indirect numerical methods are more reliable than the aforementioned experimental ones in measuring the intrinsic permeability. However, due to the high number of model parameters and the mathematical flexibility of the constitutive laws, multiple solutions can be found, specifically when experimental data-sets related to local water content distribution are not measured [13].

In this contribution, an experimental/numerical approach is proposed to characterize the hydric state and deduce the hydraulic properties of a cement-based porous medium, taking advantage of the 3D nature of the acquired neutron tomographic data sets. In section 2, the experimental campaign is described, including the sample composition, their mass loss history and the neutron tomography campaign. A number of image processing operations and a novel methodology to estimate water content based on multi-phase porous media considerations are then presented in section 2.4 and 3. This in turn allows the characterisation of the saturation gradients at different instances in time. The resulting hydric gradients are then validated against the macroscopic mass loss history provided by gravimetric experimental data sets in section 3.3.2. These hydric gradients are then used together with the mass loss measurements as a complete data set to calibrate a common numerical model in section 4 by means of a minimisation algorithm detailed in section 4.3. Once calibrated, the model allowed an indirect assessment of the intrinsic permeability and the coefficient of hydric exchange.

2. Materials and methods

The applied procedure consists of scanning multiple mortar samples having different drying period in a thermo-hydrically controlled chamber using neutron tomography. Then, a series of image processing is applied to characterize the moisture profiles in these samples. The following subsections describe the samples preparation, the drying experimental apparatus, the neutron acquisition settings and the set of image processes that were used to transform grey scale fields to moisture content fields.

2.1. Specimens

The experimental campaign presented here involves 14 samples, all made out of EN standard mortar. The water to cement ratio w/c is equal to 0.5 and the sand (standard sand CEN EN 196-1) to cement ratio s/c is equal to 3. These cylindrical samples were all cored out from a bigger bloc, which, after casting, was kept for two days in its mold in sealed conditions and was then placed in a bath of water to cure. A diamond coring bit with 12 mm inner diameter was then used to core out the samples. While one side of the samples was smooth due to its contact with the mold, the other side had to be further cut and smoothed with a rotating blade system, which was equipped with a water jet to avoid local thermal gradients. The resulting cylindrical samples had a height of 40 mm and were kept in water the beginning of the individual drying process to avoid any potential water exchanges with the environment. However, due to time constraints related to the beamline access, only 11 of 14 samples were chosen to be scanned based on their different drying periods.

2.2. Mass loss history

In order to induce different hydric states in the same material, the samples were placed at regular intervals in a drying environment. Each sample was first weighted and then rolled in three layers of adhesive aluminum tape on the longer side to avoid lateral moisture leakage and to induce a unidimensional moisture flow. The mass of aluminum tape was also measured for each sample to correct the measured mass loss. The samples were then put sequentially to dry in a thermo-hydrically controlled environment, with no ventilation, at 20 °C and 35 % relative humidity controlled with saturated $MgCl_2{,}6H_2O$ solution. The samples mass loss was characterised in time as shown in Figure 1.

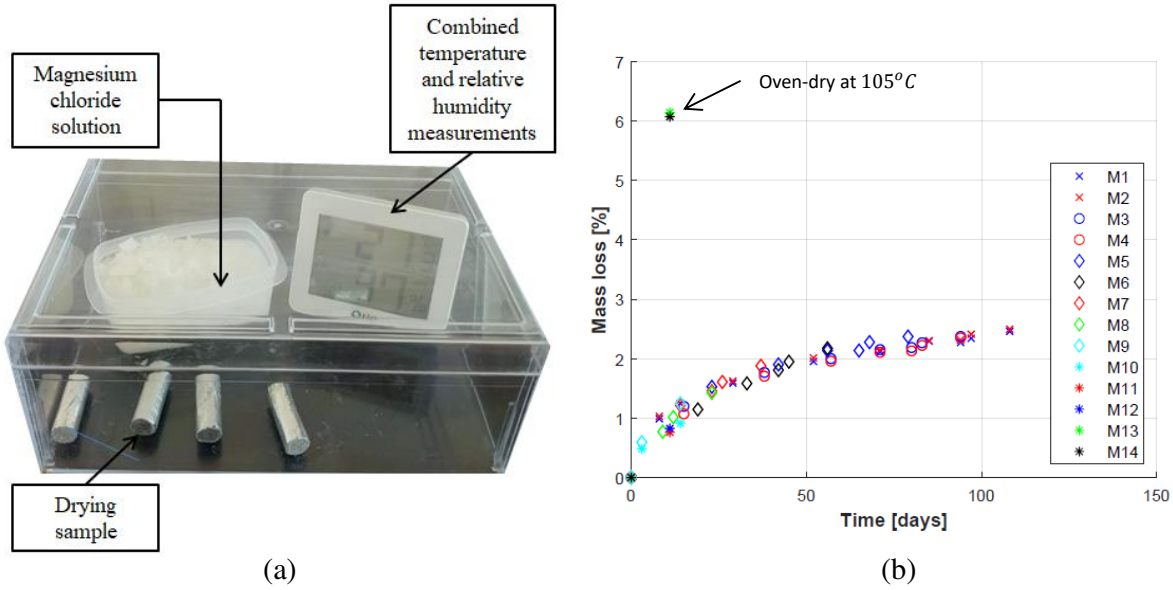

Figure 1: Drying of mortar samples: (a) Sample drying in a thermo-hydrically controlled environment (b) Total samples mass loss history

In addition, two mortar samples were put to dry in an oven set to 105 °C to obtain a reference hydric state which is key for the quantification analysis as will be shown in the next section. Given the small size of the samples, the high temperature of the environment in which they were placed, and the duration of drying of 11 days, the mass loss of these two samples is here considered to correspond to the hydric equilibrium at 105 °C.

2.3. Neutron acquisition

Similarly to x-ray, neutron imaging requires an incident beam (I_0), emitted by a source (a nuclear reactor in this case) which is collimated through a pinhole. After the interaction with the sample the beam (I) is absorbed by a scintillator, which emits visible light proportionally to the incident beam intensity. This is focused and guided by optical elements and by a sCMOS camera. A series of these radiographies (2D attenuation fields) is acquired at different angular positions of the sample. These can then be reconstructed into a 3D attenuation field e.g., through a filtered backprojection method. The neutron tomographies in this study were acquired at the NeXT-Grenoble beamline (located at the Institut Laue-Langevin (ILL) in Grenoble, France and detailed in [29]), which takes advantage of a uniquely high cold neutron flux. A schematic view of the setup is illustrated in Figure 2.

Before transporting the samples to the beamline, each sample was weighted and sealed to prevent any water exchange with the environment. Their weight was re-measured before and after each scan to ensure that no (or negligible) drying occurred during tomographic acquisition, which was found to be the case. An

identical set of neutron acquisition parameters was selected for all the tested specimens. In absence of rapid dynamic processes occurring in the samples, these parameters were optimised to maximise spatial resolution. In this case, 1088 projections were acquired in 2 hours and 54 minutes over a 360° rotation, each radiography being the average of three acquisitions, each with 3.2 seconds exposure. To achieve this, an infinity corrected optical setup was employed, coupling a 50 mm Canon Lens with a 122 mm Heliflex lens, as detailed in [29]. This setup yields a 16 µm pixel size. Given the small pixel size, a 20 µm thick $Gd_2O_2S : Tb^6LiF$ scintillator was employed, A 30 mm pinhole D (corresponding to a neutron flux of 3x10^8 ncm^{2}s at the sample, placed 10 meters away) was selected to achieve a true resolution of about 30 µm. Each neutron radiography was the average of 3 individual projections each with a 3.2 s exposure, resulting in a signal to noise $SNR = 14$.

Each set of radiographies was reconstructed into the corresponding 3D volume by means of the Feldkamp (FDK) back projection algorithm, as implemented in the commercial software X-act (from RX-Solutions). An example of a 3D neutron attenuation field of the mortar sample is reported in Figure 3.

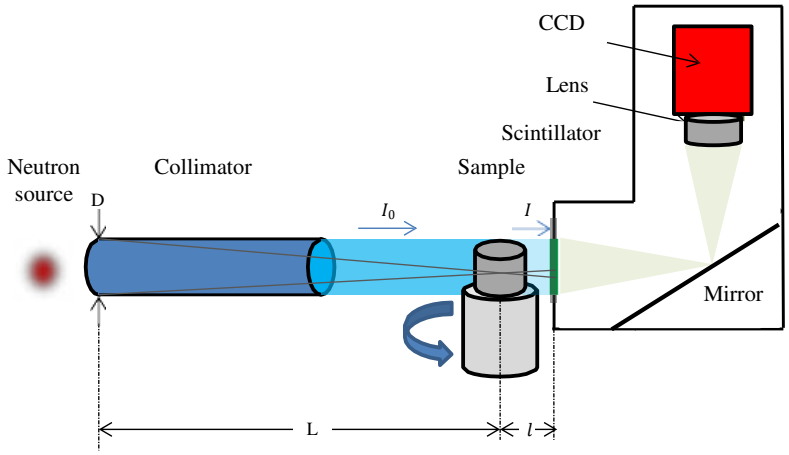

Figure 2: A schematic view of the neutron instrumentation at the NeXT-Grenoble imaging beamline.

2.4. Segmentation, labelling and particle size distribution

Moisture transport happens essentially in the interconnected porosity of the cement given the comparatively low permeability of aggregates and sand particles. Therefore, in order to isolate the contribution of this phase, it is beneficial to identify and remove these particles from the neutron tomographies. Their identification (a process named segmentation in image processing) can in this case be achieved thanks to the lower neutron attenuation (*i.e.,* the gray value of the voxels comprising them) of aggregates with respect to that of the cement paste. An histogram-based segmentation of the grains can then be achieved based on whether a voxel has a value above or below a suitably chosen threshold. In this work, to ensure repetability and avoid user dependency, this threshold was determined based on an algorithm named "$IJ\_IsoData$" [30] (available in *ImageJ* software [31]) that provides increasingly cleaner extractions of the object regions by

means of an iterative process. This method allows the identification of the aggregates from the surrounding mortar (cement paste and sand fines below the imaging resolution) as illustrated in Figure 3. Once the particles are isolated it is straightforward to "remove" them from the subsequent elaborations.

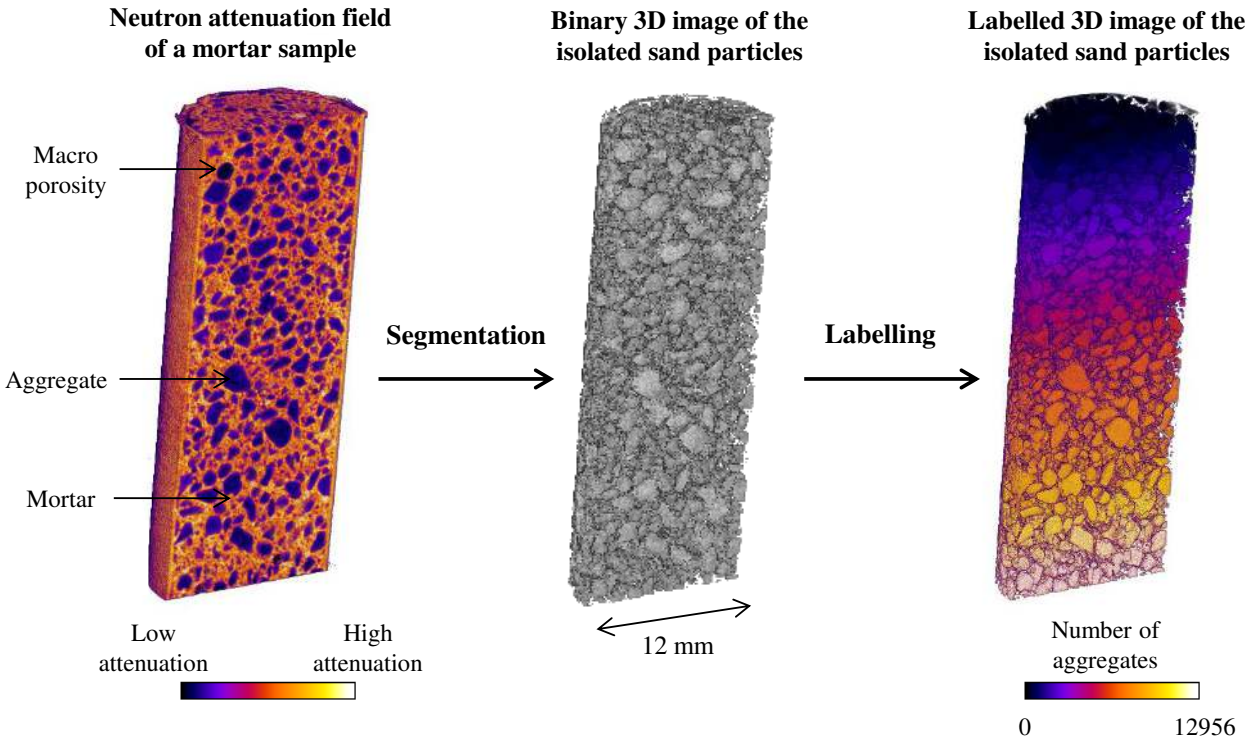

Figure 3: Segmentation and labelling processing adopted in this work. To the left: rendering of a representative 3D reconstructed attenuation field. In the middle: rendering of the binary image after histogram-based segmentation . To the right: Labelled 3D volume isolating the individual grains, whose color corresponds to the assigned incremental index.

In order to quantify for the aggregates fines that were not captured by the neutron scans resolution, a granulometric analysis was done by applying the "watershed" morphological operation [32] on the segmented image. This operation allows the separation of segmented aggregate phase into the individual grains comprising it as illustrated in Figure 3. The volume of each grain can then be measured and converted into a radius of a volume-equivalent sphere. This allows to calculate a particle size distribution as shown in Figure 4, where this cumulative probability density function is compared to the experimental sieving measurements. This comparison shows a good agreement above a 600 µm particle size.

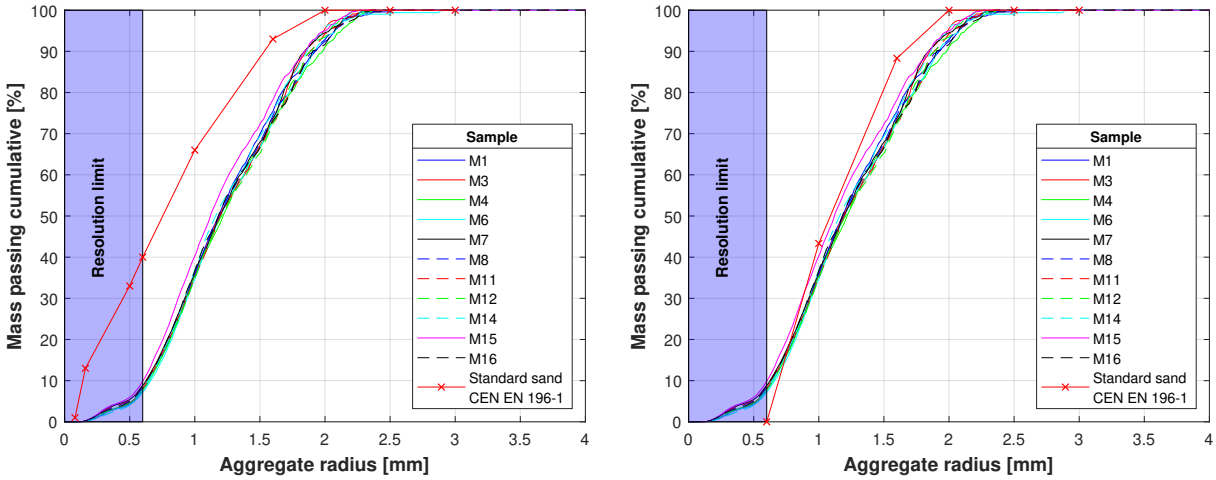

(a) Full range radii of granulometry

(b) granulometry of sand particles above 600 µm

Figure 4: A comparison between sieving-based experimental cumulative granulometry and the corresponding one estimated through image analysis, starting from 600 µm to take into account the resolution of the neutron tomography scans

3. Results

3.1. Vertical gradients

A first indication of the evolution of the moisture content due to drying is reported in Figure 5, which shows the average grayvalue over the half-height of each sample (the half being completely within the field of view, given that the sample was larger than the field of view under for the chosen resolution). Each point in the plot corresponds to the average grey value mortar voxels in a 10 pixels-thick disk, along the height of the sample. The variation of gray value attenuation shown Figure 5 can be correlated to the variation of the hydric state along the height and drying stage as shown in the next section.

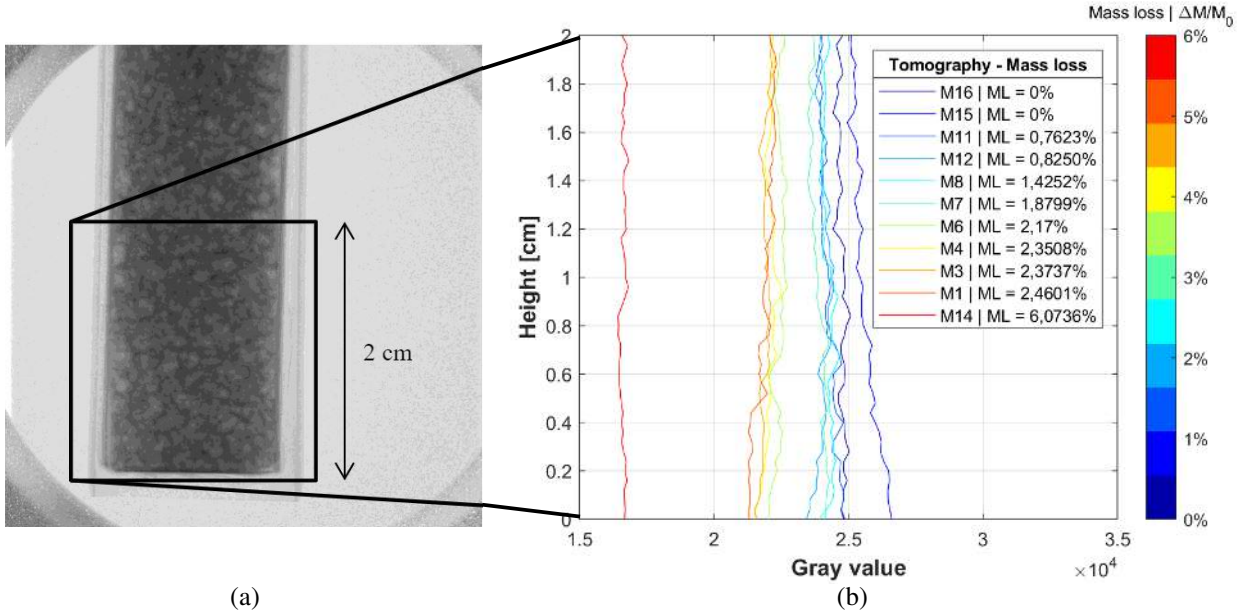

(a) (b)

Figure 5: Analysis of the attenuation profiles: (a) radiography showing the sample in the field of view (b) Grey value gradients of all the scanned samples.

From Figure 5, it can be observed that the reference samples with no mass loss (M15 and M16) show a slightly different initial water distribution. While in sample M15 the gray value attenuation profile suggests a uniform moisture content along its height, sample M16 shows an apparent moisture concentration near the top surface. This might be related to local variations in water content in between the mortar blocs from which the cylindrical samples were cored. Samples M15, M7 and M8 were in fact extracted from a different bloc different than the other samples. For this reason, in the upcoming analyses, the gray value of each sample is normalised to the corresponding reference sample cored from the same block. This measurement shows again the importance of the full-field nature of the proposed approach over the local, point-wise ones which could have led in this case to misleading conclusions.

3.2. Radial gradients

As aforementioned, the experimental campaign was conceived to impose a uni-directional drying front by sealing the lateral surface with multiple layers of aluminium tape. The three-dimensional nature of tomography allows the verification of this assumption through the study of the variation in attenuation values along the radial direction. To have a sufficient number of voxels for statistical representativity, the average over concentric (hollow) 20 slices-thick rings was compared. Additionally, the radial width of these sections was varied to maintain an almost-identical number of mortar voxels in each subvolume, as schematised in Figure 6a. The relatively small variation to voxel counts is due to the heterogeneity in aggregate content (which were removed from these statistics as detailed above). Voxel counters (red curves in Figure 6) are

employed to verify that these small variations in voxel counts don't affect the gray value profiles across the rings.

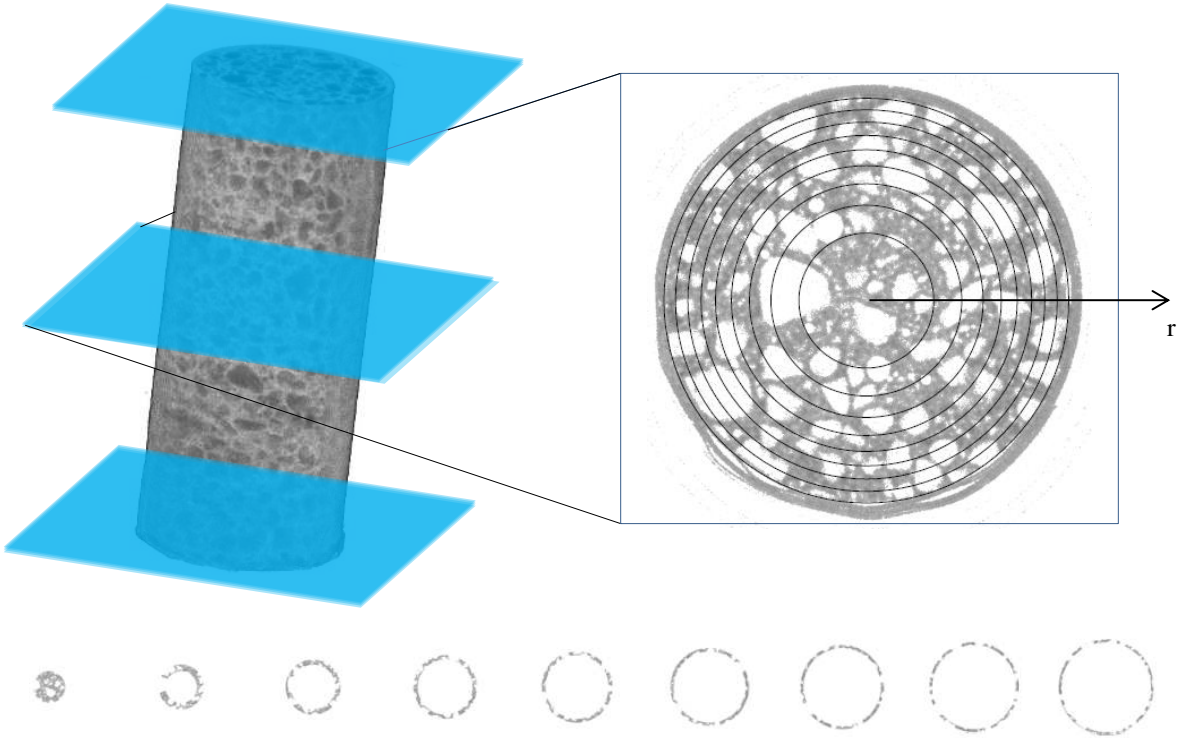

(a)

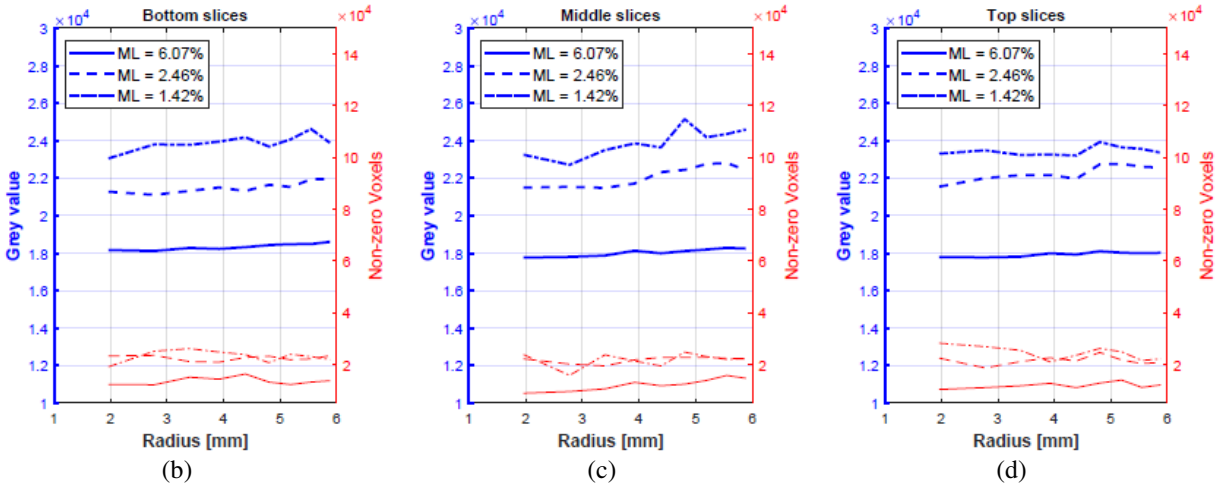

(b) (c) (d)

Figure 6: (a) Montage showing the partitioning of the sample in the radial direction so as to keep a similar number of pixels in each division. Evolution of grey value with respect to the radius for different saturation states and different positions in the sample: (b) Bottom (b) middle (c) Top

This operation was repeated at three different heights representing the top, middle and bottom of the

sample, as reported in Figure 6 b, c and d, respectively. In each of these subfigures this operation is repeated for thee representative samples at three distinct drying stages. Figure 6 shows virtually no radial gradient between the core and the external surface of the sample, in all conditions and along the height. these results are in agreement with existing previous observations in [33][34], where adhesive aluminum was found to be effective at low temperature for periods shorter than 6 months. The samples were therefore considered to be perfectly sealed, justifying the hypothesis of unidirectional drying adopted in the following sections, which will only focus on vertical gradients averaged over the sample width.

3.3. From attenuation values to saturation gradients

3.3.1. Saturation profiles

Once the aggregates are removed as detailed in section 2.4, the remaining material consists of partially saturated mortar (cement paste and sand fines below the imaging resolution). This can be further subdivided in three species: dry mortar "*dm*" (mixture of solid gel, unhydrated cement, chemically-bonded water and sand fines), capillary water "*cw*" and air "*a*".

The gray value (measured attenuation) of the mortar, considered as a multiphase mixture "*mix*" can be therefore expressed as the sum of these individual components:

$$\mu_{mix} = W_{cw}\mu_{cw} + W_a\mu_a + W_{dm}\mu_{dm}, \tag{1}$$

where W_i and μ_i are respectively the volumetric fraction and the intrinsic gray value of the specie i.

Assuming that the dry mortar undergoes a negligible mass variation (*i.e.,* negligible effect of the dehydration reaction) and neglecting any contribution to the gray value induced by the modest volumetric variation (*e.g.,* drying shrinkage), the variation of the compound attenuation between two saturation states can then be expressed as:

$$\Delta\mu_{mix} = \Delta W_{cw}\mu_{cw} + \Delta W_a\mu_a, \tag{2}$$

where the increase in the volumetric fraction of air is equal to the reduction of water ($\Delta W_a = -\Delta W_{cw}$) since the moisture leaving the porosity is replaced by air. The variation of capillary water volume fraction writes then:

$$\Delta W_{cw} = \frac{\Delta\mu_{mix}}{\mu_{cw} - \mu_a} \tag{3}$$

The gray value of air μ_a can be directly measured in the tomographies and was found to average 7900 (gray value) with a standard deviation σ_a of 1000. On the other hand, the gray value of water μ_w was measured in multiple water-filled macro pores in the reference samples. It averaged 50500, with a standard deviation of 2000. It should be noted, nonetheless, that this value can slightly vary depending on the hydric state of the material, because of the scattering contribution to the attenuation. The attenuation law of water can in fact diverge from the beer-Lambert law, as generally the case for highly scattering elements in high

concentration. For the specific energy spectrum of the used NeXT beamline, this discrepancy from the Beer Lambert was measured, for example, in [35]. A possible approach to correct for this spurious fluctuation is then to account for a correction based on the observed correlation between equivalent water thickness "x" and water attenuation contribution, as measured on a reference, water-filled wedge sample. For thicknesses between 0 mm and 4 mm this can be fit with a second order polynomial $\mu_w(x) = ax^2 + bx + c$, where for this beamline $a = -0.0052$, $b = -0.0023$ and $c = 0.3107$. Assuming that this correction, measured in radiography, is also valid in tomography, the water gray value varies then non-linearly between 50500 and 57000 in between the reference, wet state and and ultimate, oven dry state.

The estimation of a saturation profile from capillary water volumetric fraction can be expressed as:

$$S_l = S_l^i - \Delta S_l = S_l^i - \frac{\Delta W_{cw}}{\widehat{\Phi}_m} \tag{4}$$

Where S_l is the saturation to liquid water, S_l^i is the initial, reference saturation, *i.e.*, the early-age saturation after correcting for self-desiccation that reduces the fresh concrete relative humidity. $\widehat{\Phi}_m$ is the average porosity of the mortar phase after removal of the larger particles, as detailed above.

The volumetric fraction of fines ξ_f below the resolution of the approach is estimated to be 40%, based on the granulometric analysis in section 2.4. thereby, the averaged porosity of the mortar after segmentation (cement and sand fines) can be estimated by interpolating between cement paste porosity and mortar porosity (with full granulometry), the interpolation coefficient being the fines volume fraction ξ_f, it follows that:

$$\widehat{\Phi}_m = \phi_{cp} - \xi_f(\phi_{cp} - \phi_m) \tag{5}$$

where ϕ_m is the mortar porosity, equal to 16%, and ϕ_{cp} is the cement paste porosity estimated to 37% as reported in [36] for the same types of material.

To finally deduce the saturation in Eq. 4, the only remaining parameter to determine is the initial saturation. To deduce this initial value, which can fluctuate depending on the exact sample history, the final, oven dried state (which is instead far more stable) was used as a reference. It should in fact be noted that variations in the choice of the initial saturation shift the ΔS_l profiles to lower or higher absolute hydric states but do not affect the overall water loss along the tests. The initial saturation was then chosen to be 78% for all samples (despite the possible fluctuations between them), so as to ensure a saturation of less than 10% in the oven-dry states, as highlighted in Figure 7. This 10% limit was measured in [37],[38] in similar cementitious materials adopting a combined experimental and thermodynamics-based theoretical characterization of desorption isotherms up to moderate temperatures.

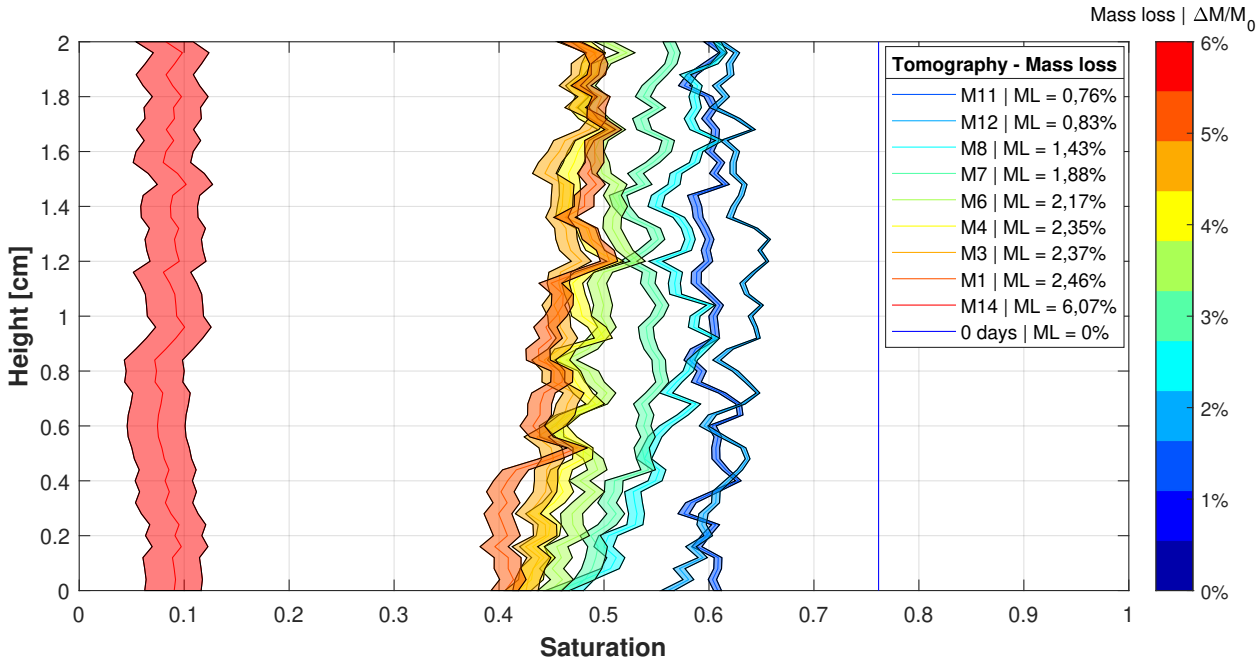

Figure 7: Neutron-based measurement of saturation gradients of mortar samples at different hydric states. The measurement accounts for the variability of the fluids gray value attenuation coefficients.

The saturation profiles in Figure 7 show an overall gradient in between the upper exchange surface and the core of the sample up to 10%. This relatively weak saturation gradient is expected, given the lack of ventilation in the drying controlled environment. The additional local gradients along the samples' heights suggest local saturation variability in the porous networks of the samples.

3.3.2. Validation of mass loss measurements

The robustness of the grayvalue-saturation transition can be verified comparing it to the overall mass loss measured macroscopically over the whole sample via gravimetric analysis. While lacking the spatial information, in fact, this measurement is robust, and can be compared to the integral of the mass loss along the height of each sample. Specifically, mass loss can be calculated from each saturation profile S_l^t measured after a drying-period t and its difference from the reference initial saturation profile S_l^0 as:

$$\Delta M_t = \frac{\rho_l . \widehat{\Phi}_m \int_0^l (S_l^0 - S_l^t)}{\rho_m^{sat}}, \tag{6}$$

where ρ_l is the water density, $\widehat{\Phi}_m$ is the averaged porosity of the mortar after removing the bigger particles as detailed above and ρ_m^{sat} is the density of mortar accounting for the full granulometry. The so-deduced mass loss for all the scanned samples, compared to the balance measurements is reported in Figure 8. The error bars for the imaging-based approach, show the effect of the aforementioned variability in the coefficient

of attenuation of water and air. Despite the specificity in the composition of each sample, which can induce hydric variability as well as all the assumption previously stated, the gravimetry-based and tomography-based measurements are in good agreement.

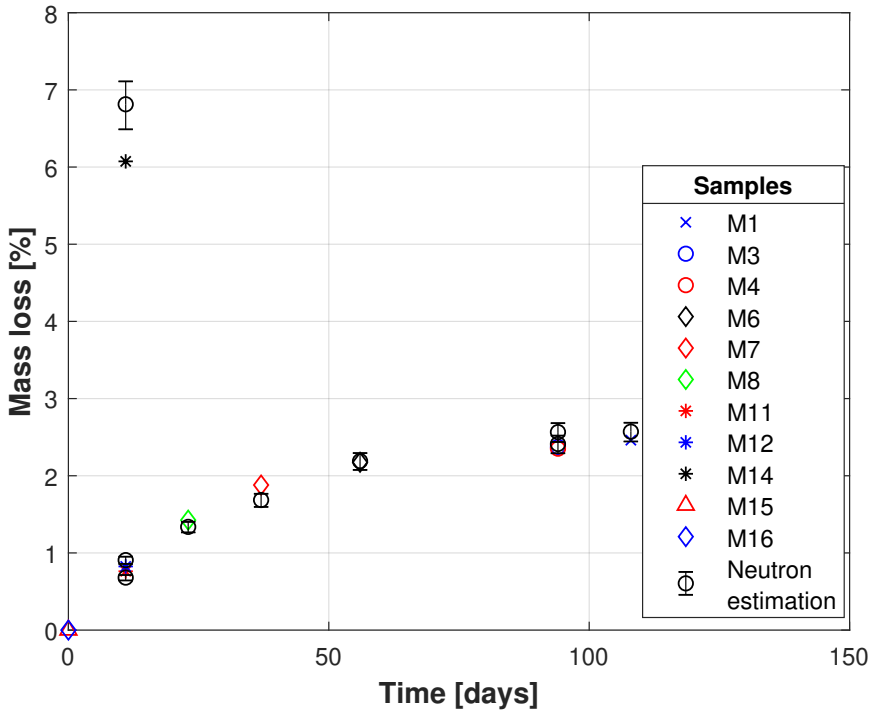

Figure 8: Comparison between the balance-measured mass loss and the one deduced from image analysis.

4. Modeling of moisture transfer

To complete the characterisation of the processes at play, numerical models are of key importance to identify crucial hydraulic parameters, such as the intrinsic permeability and the coefficient of hydric exchange. It is in fact possible to identify those parameters once the model is calibrated not only to the macroscale mass loss dataset but also the spatio-temporal gradients made available by the presented experimental campaign.

Several numerical models have been proposed in the literature to describe moisture transport in unsaturated porous media. They can be broadly classified into two main categories: complete and simplified models. While models belonging to the former establish a rigorous description of all the species of interest (liquid water, vapor and dry air) [39][40], models belonging to the latter propose a set of assumptions that simplify the physical description of the involved processes. This set of simplification generally remains valid when the gas pressure in the interconnected porosity remains equal to the atmospheric pressure, which means that all local pressure buildups dissipate quasi-instantaneously and the liquid permeation remains the

dominant water transport mechanism. In this work, given the drying conditions imposed in the controlled environment (drying temperature of 20 °C and relative humidity of 35%), and given the material adopted (mortar having a water to cement ratio of 0.5), we assume the validity of a simplified model [41] [28].

4.1. Numerical model

The simplified model adopted derives from the mass conservation equation of the liquid water in the porous system, expressed as:

$$\frac{\partial m_l}{\partial t} + \boldsymbol{\nabla} \cdot (m_l v_{l-s}) = 0, \tag{7}$$

where m_l is the mass of liquid water and v_{l-s} is the velocity of the liquid water with respect to the solid skeleton of the material. The mass of water can be expressed in terms of density ρ_l, porosity ϕ and liquid saturation rate S_l as:

$$m_l = \rho_l S_l \phi \tag{8}$$

whereas its velocity with respect to the solid skeleton can be computed using Darcy's law:

$$v_{l-s} = -K \frac{k_{rl}}{\mu_l} \nabla p_l, \tag{9}$$

where K, k_{rl} and μ_l are the intrinsic permeability of the system, the relative permeability of liquid water and its dynamic viscosity, respectively. Assuming the incompressibility of water, (ρ_l = cte), as well as the existence of a differentiable function between saturation and capillary pressure, the conservation equation reads:

$$\left[\phi \frac{\partial S_l}{\partial p_c}\right] \frac{\partial p_c}{\partial t} - \boldsymbol{\nabla} \cdot \left[\left(\frac{k_{rl}(S_l) K}{\mu_l}\right) \nabla p_c\right] = 0 \tag{10}$$

This equation requires the definition of four quantities: porosity ϕ, a differentiable function of saturation, function of the capillary pressure $S_l(p_c)$, as well as intrinsic permeability K and relative permeability k_{rl}. Assuming that the hydration reaction of cement ended before the samples were exposed to drying, the microstructural properties, and in particular porosity and intrinsic permeability can be assumed as constant. The water retention curve (desorption isotherm) can be described by the Van Genuchten family of equations [42]:

$$S_l(p_c) = \left[\left(-\frac{p_c}{a}\right)^{\frac{1}{1-\frac{1}{b}}} + 1\right]^{-\frac{1}{b}}, \tag{11}$$

where the parameters a and b are fitting parameters. The Mualem [1] model is also used here to describe the relative permeability to liquid water as a function of water saturation:

$$K_{rl} = \sqrt{S_l}\left(1 - \left(1 - S_l^b\right)^{1/b}\right)^2 \tag{12}$$

By analogy to the differential equation for heat transfer, it is possible to name $\left(\phi \frac{\partial S_l}{\partial p_c}\right)$ the hydraulic capacity and $\left(\frac{K k_{rl}}{\mu_l}\right)$ the hydraulic conductivity. Equation (10) is here discretized and solved using the finite software Cast3m, and specifically its heat module accounting for the non-linear hydric conductivity term

which depends on capillary pressure solution. The temporal discretization is done using the theta-method scheme.

4.2. Model inputs, initial and boundary conditions:

A quarter of the sample was described in axisymmetric conditions. A total of 182 eight-node elements were used for meshing the 2D surface, which was refined near the imposed boundary condition to ensure better convergence and higher results accuracy as shown in Figure 9.

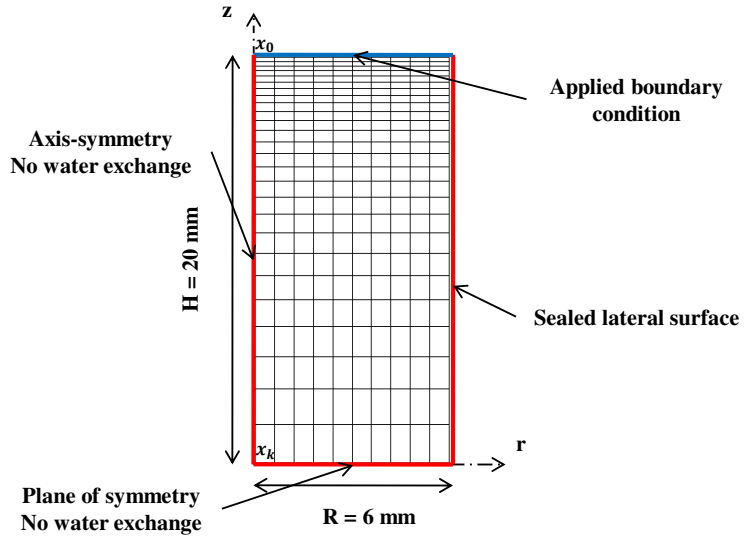

Figure 9: Scheme of the adopted finite element mesh and boundary conditions.

Two types of boundary conditions are generally employed in this kind of model to impose environmental conditions. The first is Dirichlet boundary condition, which consists of imposing the relative humidity of a surface (or an equivalent quantity, depending on the primary variable of the differential equation employed). For example this could be used to impose the relative humidity within the environmental chamber directly at the exposed air-concrete interface. Nonetheless, this approach usually overestimates the interface exchanges, and neglects the presence of the so-called boundary-layer, whose moisture content evolves gradually depending on the distance to the material surface. The extent of this boundary-layer depends on the temperature of the chamber, the ventilation, as well as on the surface condition of the material. A second possible type of boundary conditions, are the Neumann-type boundary conditions, which can be generally expressed as:

$$\overrightarrow{J_{bc}} = h_{bc}.(p_c^s - p_c^e).\overrightarrow{n}, \tag{13}$$

where p_c^s and p_c^e are the equivalent surfacic and external capillary pressures, respectively. $\overrightarrow{J_{bc}}$ is the water flux and h_{bc} is the convective exchange coefficient. This last parameter has a large variability (up to 4 orders of

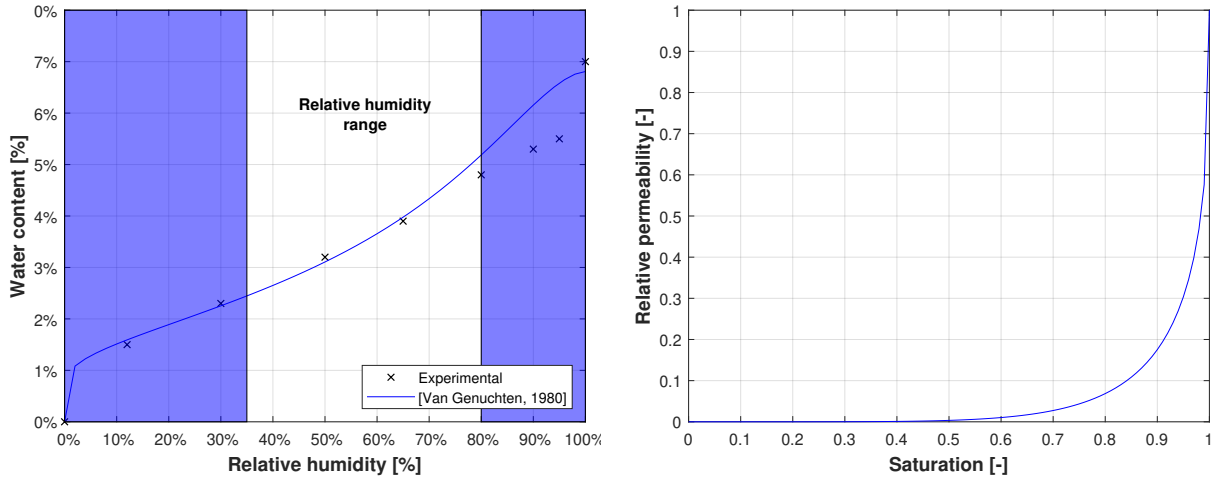

(a) Numerical vs. experimental desorption isotherm

(b) Relative Permeability

Figure 10: The desorption isotherm and the relative permeability behavior laws required for the model closure.

magnitude), depending on the material and the experimental conditions [43] [44]. In the specific conditions of this experimental campaign, however, due to the low ventilation, it is expected to be small.

As mentioned in section 4.1, the model requires the definition of four quantities, namely porosity ϕ, a differentiable function of saturation with respect to capillary pressure $S_l(p_c)$, intrinsic permeability and relative permeability. All these properties were characterized experimentally in [36], which has been used as a reference, with the exception of the intrinsic permeability (and more precisely, the permeability to water). The initial relative humidity value is assumed equal to 80%, which corresponds to an initial saturation state of 78%, as deduced above. The correspondence between relative humidity and saturation is based on the desorption isotherm reported in [36].

4.3. Model calibration and identification of hydraulic properties

Beside the aforementioned material properties, the model requires two additional fitting constants a and b, which influence the shape of the $S_l(p_c)$ and $K_{rl}(S_l)$ functions. Desorption isotherms for this class of materials were proposed in [36], but, to the best of the the authors' knowledge, no direct experimental characterization of the relative permeability of the studied class of materials is proposed in the literature. The parameter b, identified in the van Genuchten law, was therefore taken the same in the Mualem function for sake of consistency.

Once the isotherms are fitted against the dataset in [36] and the consequent relative permeability function is identified, two parameters remain to be defined: the intrinsic permeability K and coefficient of hydric convection h_{bc}. For this purpose, an optimisation procedure was implemented. It consists of minimising the error between the experimental and numerical response surfaces in the $[K, h_{bc}]$ two-dimensional space. The

goal is to find the values of K and h_{bc} that minimize the total experimental/numerical error. This total error is composed of 3 normalized independent sub-errors defined as follow: the first sub-error computes the difference between the numerical mass loss output and the experimental one, averaged over the time steps. The second sub-error computes the difference between the numerical saturation values and the experimental ones (previously shown in Figure 7), averaged over all the nodes on the geometric line $[x_0, x_k]$ (see Figure 9) and then over all the time steps on which the measurements were done. Finally, the last sub-error computes the difference between numerical and experimental saturation "average slope", averaged over time. This "average slope" considers the saturation gradient as a line delimited by x_0, where $S_l^{x_0} = S_l^{max}$, and x_k, where $S_l^{x_k} = S_l^{min}$. The system of equations of the numerical/experimental errors reads:

$$\begin{cases} \underbrace{\sum_{t_i=t_0}^{t_n} \frac{\left|\frac{\Delta M_{exp}^{t_i} - \Delta M_{num}^{t_i}}{\Delta M_{exp}^{t_i}}\right|}{n}}_{\substack{\text{Mass loss} \\ \text{cumulative error}}} < \boldsymbol{\alpha} \\ \underbrace{\sum_{t_i=t_0}^{t_n} \frac{1}{n}\left(\sum_{x_j=x_0}^{x_k} \frac{\left| S_{l\,num}^{x_j,t_i} - S_{l\,exp}^{x_j,t_i} \right|}{k} \right)}_{\substack{\text{Saturation values} \\ \text{cumulative error}}} < \boldsymbol{\beta} \\ \underbrace{\sum_{t_i=t_0}^{t_n} \frac{\left|(S_{l\,num}^{x_k,t_i} - S_{l\,num}^{x_0,t_i}) - (S_{l\,exp}^{x_k,t_i} - S_{l\,exp}^{x_0,t_i})\right|}{n}}_{\substack{\text{Saturation profiles' slopes} \\ \text{cumulative error}}} < \boldsymbol{\gamma} \end{cases} \tag{14}$$

Where $\Delta M_{exp}^{t_i}$ and $\Delta M_{num}^{t_i}$ are respectively the experimental and numerical mass loss at the time step t_i, n is the total number of time steps, $S_{l\,num}^{x_j}$ and $S_{l\,exp}^{x_j}$ are respectively the numerical and experimental saturation at the node x_j which belongs to the line $[x_0, x_k]$ going from the surface to the core of the sample. $\boldsymbol{\alpha}, \boldsymbol{\beta}, \boldsymbol{\gamma}$ are the threshold factors under which the constraint is full field, specifically, $\boldsymbol{\alpha}$ is the threshold factor for the mass loss dataset, $\boldsymbol{\beta}$ and $\boldsymbol{\gamma}$ are respectively the threshold factor for the saturation value and the saturation slope data-set. The value of these threshold parameters are to be chosen by the user and depends on the tolerance he sets to achieve a satisfying fitting. In here, for instance, we assume that any mass loss error below 0.25% gives a satisfying fitting.

The key steps in the modelling approach and the experimental/numerical error minimization procedure are illustrated in Figure 11.

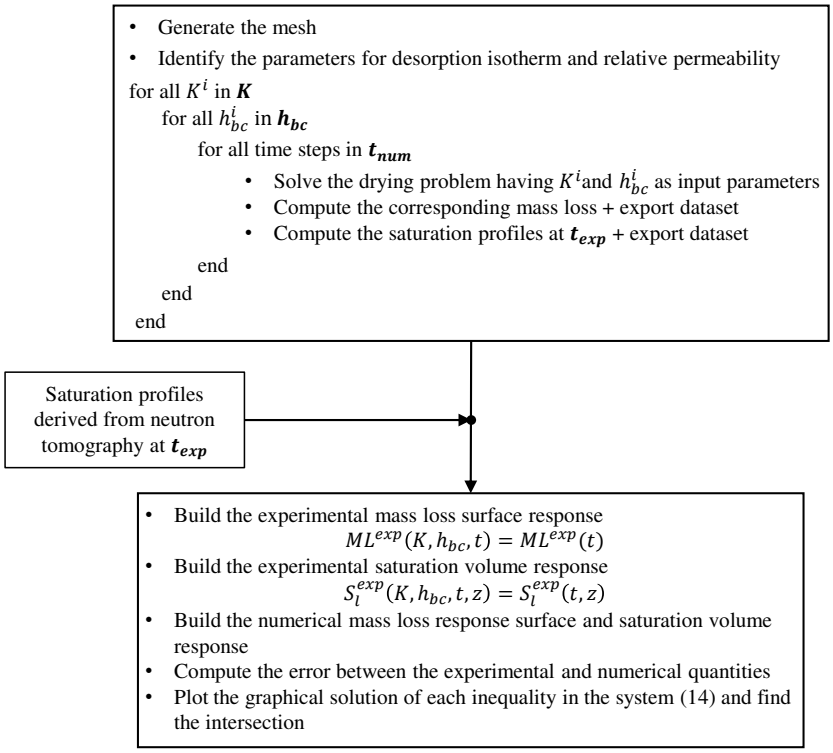

Figure 11: Flowchart detailing the modelling approach and the experimental/numerical error minimization procedure.

The minimization procedure output is visualized in Figure 12. On the left, the evolving numerical and experimental mass loss surfaces in $[K, h_{bc}]$ space are visualized at a specific time step, here, at 109 days. Each node of the numerical mass loss surface represents the mass loss output of the simulation having the corresponding $[K, h_{bc}]$ as input parameters. As to be expected, this surface shows a minimum when h_{bc} and K have there lowest value in the space, *i.e.*, at $K = 4 \times 10^{-21}$ and $h_{bc} = 0.1$ and shows a maximum at $K = 5 \times 10^{-20}$ and $h_{bc} = 3.5$. On the other hand, the experimental mass loss response surface in this plot is represented by a constant horizontal surface in the $[K, h_{bc}]$ space at each specific time step. This constant value corresponds to the interpolated mass loss value of the previously shown curve in Figure 1 at the corresponding numerical time steps. In the middle, the mass loss cumulative error response surface is shown together with the sets of $[K, h_{bc}]$ that fulfills the first inequality in the equation 14. This set of points can be also represented by a polygon that joins the points on the boundary of the formed shape. Finally, on the right, the graphical solution of each inequality in equation 14 is plotted. It was found that the intersection of these 3 polygons is a point that corresponds to a permeability K value equal to 10^{-20} and to a coefficient of hydric exchange h_{bc} equal to 0.4. The value of h_{bc} was found to be one/two order(s) of magnitude smaller than reported in other studies (*e.g.,* [45]). This is likely caused by the lack of ventilation in the environmental control chamber. On the other hand, the value of K is marginally higher than the

common estimation of this parameter. This discrepancy might be also attributed to the simplified nature of the adopted model which only accounts for the permeation of liquid water, neglecting the contribution of the diffusion of vapour. In fact, the low value of coefficient of hydric exchange slows the kinetics of the process, allowing a slow diffusion of vapor to take place in the porosity. The identified value of "K" is therefore the cumulative result of two distinct water transport processes: liquid water permeation and vapor diffusion. On the other hand, unlike other studies, the neutron tomographies acquired inhere allows for a direct measurement of saturation profile which is a more reliable dataset for the numerical fitting in comparison to other methods in the literature. Moreover, the suggested minimization procedure allows for a more objective fitting and for a more accurate identification for the hydraulic parameters than what can be found in different studies.

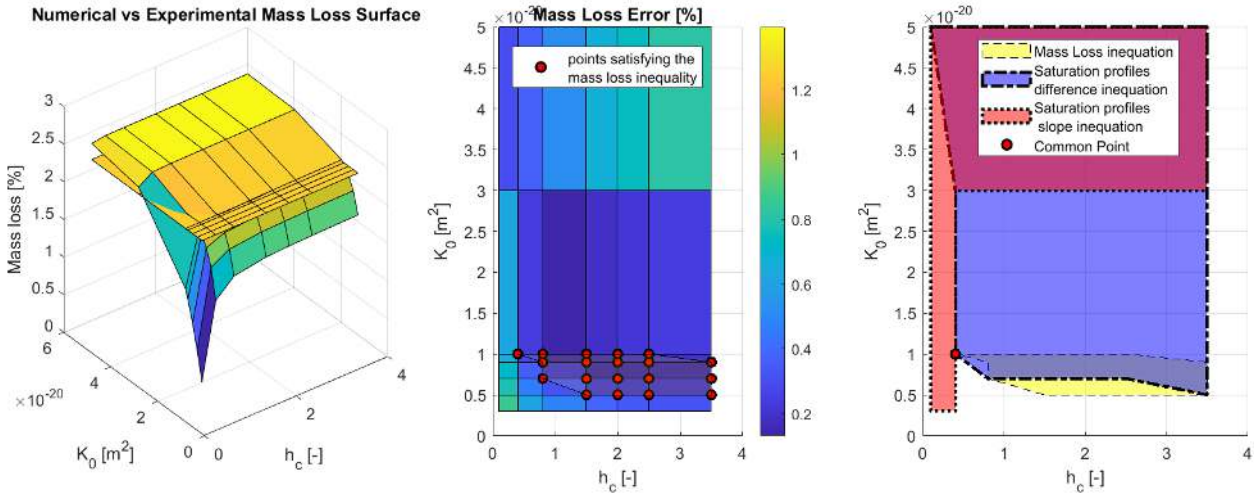

Figure 12: Minimization procedure: (Left) numerical and experimental mass loss response surfaces in $[K, h_{bc}]$ space at 109 days, (Middle) cumulative mass loss error surface together with the sets of $[K, h_{bc}]$ fulfilling the mass loss inequality, (Right) Graphical solutions of all the inequalities in equation 14 which intersect at $[K = 10^{-20}, h_{bc} = 0.4]$.

Using the values of $[K, h_{bc}]$ identified by the minimization procedure, the mass loss and saturation gradients numerical outputs are plotted against experimental data in Figure 13 and Figure 14, which shows a good agreement, within experimental error.

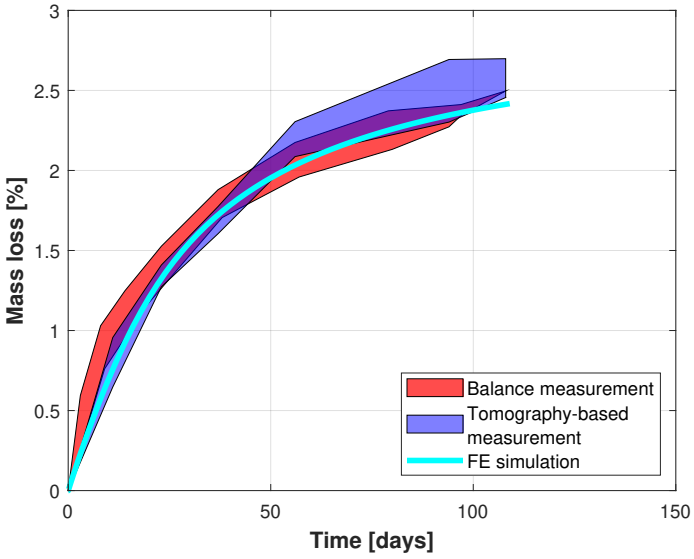

Figure 13: Mass loss comparison of the: (red) balance measurements, (blue) image-based measurements and (cyan) FE estimation. The shaded area being to account for the variability of the acquired measurements.

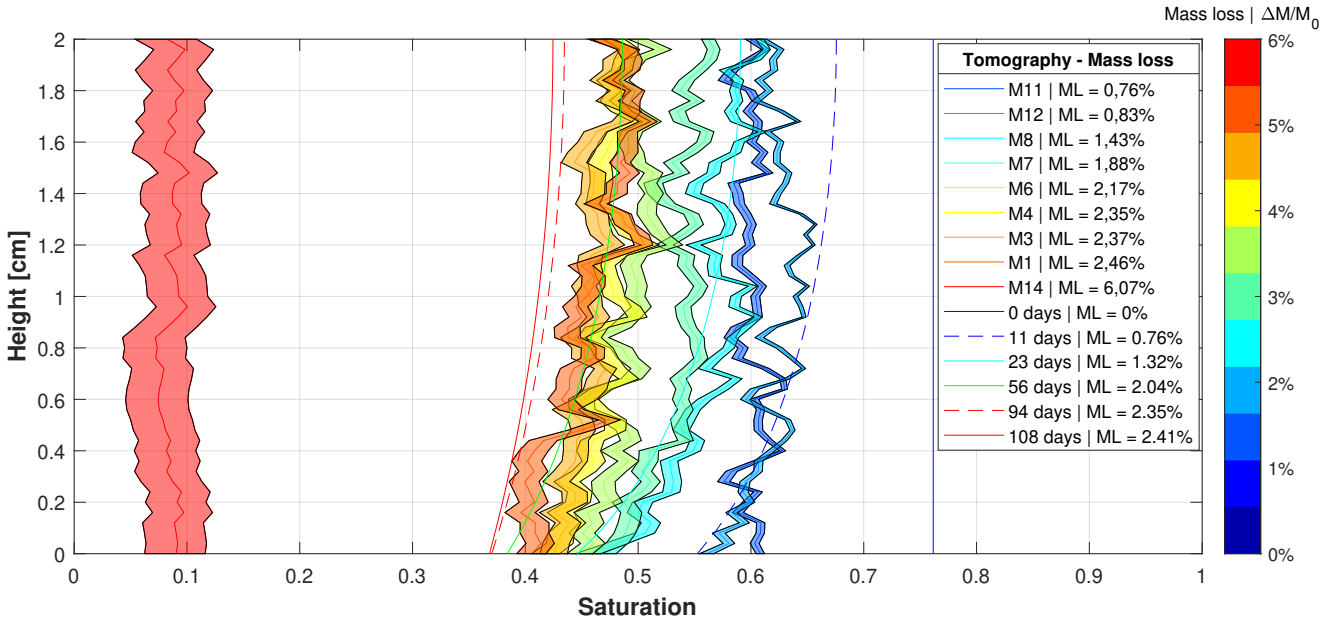

Figure 14: Saturation gradients: (shaded) image-based estimations accounting for the variability f the acquired measurement, (solid and dashed) FE estimations.

5. Conclusions

In this paper, an experimental-numerical approach was proposed to fully characterize the hydric state and properties of cement-based porous media. The novel aspect of this work lies in the adoption of neutron tomography to characterise the drying of cement-based materials at ambient temperatures with a major focus on measuring and validating water content profiles.

A set of 11 laterally-sealed cylindrical samples were dried in a thermo-hydrically controlled chamber for different time spans, while monitoring their weight loss along time. A high resolution neutron tomography was then acquired for each sample. The key phases were then differentiated in the images and their contribution to the overall neutron attenuation of the mixture was calculated. This allowed the estimation of the spatial distribution of water for different drying times with respect to a reference, wet sample. Based on an estimation of the initial saturation and the porosity of the material, it was then possible to deduce the saturation profiles to liquid water. These showed a gradient up to 10% between the exposed top surface and the core of the sample. The overall water loss of each sample deduced from the image-based saturation profiles and was also validated against the macroscopic mass loss derived from weight measurements.

After characterizing the spatio-temporal hydric state of the material, *i.e.* mass loss history and saturation gradients, a simplified finite element model was used to reproduce these experimental datasets and therefore identify key hydraulic parameters such as permeability K and coefficient of hydraulic conductivity h_{bc}. In addition, a minimization procedure was developed to ensure a more objective fitting procedure and to carefully assess the identification of those parameters. The numerical output were compared to the experimental ones and shows a fair agreement within the experimental error margin.

6. Data availability statement

The raw neutron tomography data-sets of the mortar samples will be available for ILL user club members in 3 to 5 years time at:
`https://data.ill.fr/proposal/getfile?file=201/d50tomo/exp_UGA-98/rawdata` - the analyzed experiment are in folders 01_M1, 02_M7, 03_M11, 05_M14, 06_M15, 07_M6, 08_M16, 09_M8, 10_M4 and 12_M3.

References

[1] Y. Mualem, A new model for predicting the hydraulic conductivity of unsaturated porous media, Water Resources Research 12 (3) (1976) 513–522. doi:10.1029/WR012i003p00513.

[2] P. Perre, A. Degiovanni, Simulation par volumes finis des transferts couplés en milieux poreux anisotropes: Séchage du bois à basse et à haute température, International Journal of Heat and Mass Transfet (1990) 2463–2478.

[3] G. Sciumè, F. Benboudjema, C. D. Sa, Y. Berthaud, B. Schrefler, A multiphysics model for concrete at early age applied to repairs problems, Engineering Structures 57 (2013) 374–387.

[4] J. Pan, Y. Feng, J. Wang, Q. Sun, C. Zhang, D. Owen, Modeling of alkali-silica reaction in concrete: A review, Frontiers of Structural and Civil Engineering 6. doi:10.1007/s11709-012-0141-2.

[5] P. Baggio, C. Bonacina, M. Strada, Trasporto di calore e massa nel calcestruzzo cellulare., La Termotecnica (1993) 53 –60.

[6] Z. Bazant, J. Chern, Concrete creep at variable humidity: constitutive law and mechanism, Materials and structures 18 (1985) 1–20.

[7] D. Dauti, A. Tengattini, S. Dal Pont, N. Toropovs, M. Briffaut, B. Weber, Analysis of moisture migration in concrete at high temperature through in-situ neutron tomography, Cement and Concrete Research 111 (2018) 41–55.

[8] A. Tengattini, S. Dal Pont, H. Cheikh Sleiman, F. Kisuka, M. Briffaut, Quantification of evolving moisture profiles in concrete samplessubjected to temperature gradient by means of rapid neutron-tomography: influence of boundary conditions, hygro-thermalloading history and spalling mitigation additives., Strain.

[9] V. Baroghel-Bouny, Caractérisation microstructurale et hydrique des pâtes de ciment et des bétons ordinaires et à très hautes performances., Ph.D. thesis, Ecole Nationale des Ponts et Chaussées. (1994).

[10] V. Baroghel-Bouny, M. Mainguy, T. Lassabatere, O. Coussy, Characterization and identification of equilibrium and transfer moisture properties for ordinary and high-performance cementitious materials, Cement and Concrete Research 29 (8) (1999) 1225 – 1238. doi:https://doi.org/10.1016/S0008-8846(99)00102-7.

[11] J. Kim, C. Lee, Moisture diffusion of concrete considering self-desiccation at early ages, Cement and Concrete Research 29 (12) (1999) 1921 – 1927. doi:https://doi.org/10.1016/S0008-8846(99)00192-1.

[12] X. Ma, J. Carette, F. Benboudjema, R. Bennacer, Optimization of experiment methodology based on identification of parameters in concrete drying, Construction and Building Materials 256 (2020) 119421. doi:https://doi.org/10.1016/j.conbuildmat.2020.119421.

[13] J. Carette, F. Soleilhet, F. Benboudjema, R. Bennacer, A. Darquennes, K. Abahri, G. Nahas, Identifying the mechanisms of concrete drying: An experimental-numerical approach, Construction and Building Materials 230. doi:10.1016/j.conbuildmat.2019.117001.

[14] G. Viggiani, S. A. Hall, E. Romero, Advanced experimental techniques in geomechanics, Alert Doctoral School.

[15] G. Viggiani, A. Tengattini, Recent developments in laboratory testing of geomaterials with emphasis on imaging, 2019. doi:10.32075/17ECSMGE-2019-1112.

[16] P. Faure, S. Caré, C. Po, S. Rodts, An MRI-SPI and NMR relaxation study of drying-hydration coupling effect on microstructure of cement-based materials at early age, Magnetic resonance imaging 23 (2005) 311–4. doi:10.1016/j.mri.2004.11.034.

[17] M. Fourmentin, P. Faure, S. Rodts, U. Peter, D. Lesueur, D. Daviller, P. Coussot, Nmr observation of water transfer between a cement paste and a porous medium, Cement and Concrete Research 95 (2017) 56 – 64. doi:https://doi.org/10.1016/j.cemconres.2017.02.027.

[18] P. McDonald, O. Istok, M. Janota, A. Gajewicz-Jaromin, D. Faux, Sorption, anomalous water transport and dynamic porosity in cement paste: a spatially localised 1H NMR relaxation study and a proposed mechanism, Cement and Concrete Research 133 (2020) 106045.

[19] G. Villain, M. Thiery, Gammadensimetry: A method to determine drying and carbonation profiles in concrete, Ndt E International - NDT E INT 39 (2006) 328–337. doi:10.1016/j.ndteint.2005.10.002.

[20] A. Voss, Imaging moisture flows in cement-based materials using electrical capacitance tomography, Ph.D. thesis, University Of Eastern Finland (2020).

[21] R. Loubser Du Plooy, G. Villain, S. P. Lopes, A. Ihamouten, X. Derobert, Electromagnetic non-destructive evaluation techniques for the monitoring of water and chloride ingress into concrete: a comparative study, Materials and Structures 48 (2015) 369–386.

[22] E. Perfect, C.-L. Cheng, M. Kang, H. Bilheux, J. Lamanna, M. Gragg, D. Wright, Neutron imaging of hydrogen-rich fluids in geomaterials and engineered porous media: A review, Earth-Science Reviews 129 (2014) 120 – 135. doi:https://doi.org/10.1016/j.earscirev.2013.11.012.

[23] P. Zhang, F. H. Wittmann, P. Lura, H. S. Muller, S. Han, T. Zhao, Application of neutron imaging to investigate fundamental aspects of durability of cement-based materials: A review, Cement and Concrete Research 108 (2018) 152–166.

[24] A. Tengattini, N. Lenoir, E. Andò, G. Viggiani, Neutron imaging for geomechanics: A review, Geomechanics for Energy and the Environment (2020) 100206doi:https://doi.org/10.1016/j.gete.2020.100206.

[25] E. Stavropoulou, E. Ando, E. Roubin, N. Lenoir, A. Tengattini, M. Briffaut, P. Besuelle, Dynamics of water absorption in callovo-oxfordian clayrock revealed with multimodal x-ray and neutron tomography, Frontiers in Earth Science 8 (2020) 6. doi:10.3389/feart.2020.00006.

[26] H. Cheikh Sleiman, A. Tengattini, M. Briffaut, B. Huet, S. Dal Pont, Simultaneous x-ray and neutron 4d tomographic study of drying-driven hydro-mechanical behavior of cement-based materials at moderate temperatures, Cement and Concrete Research 147 (2021) 106503. doi:https://doi.org/10.1016/j.cemconres.2021.106503.

[27] S. Rahimi-Aghdam, M. Rasoolinejad, Z. Bazant, Moisture diffusion in unsaturated self-desiccating concrete with humidity-dependent permeability and nonlinear sorption isotherm, Journal of Engineering Mechanics 145. doi:10.1061/(ASCE)EM.1943-7889.0001591.

[28] H. Cheikh Sleiman, M. Briffaut, S. Dal Pont, A. Tengattini, B. Huet, Influence of common simplifications on the drying of cement-based materials up to moderate temperatures., International Journal Of Heat And Mass Transfer (2020) 119254.

[29] A. Tengattini, N. Lenoir, E. Andò, B. Giroud, D. Atkins, J. Beaucour, G. Viggiani, Next-grenoble, the neutron and x-ray tomograph in grenoble, Nuclear Instruments and Methods in Physics Research Section A: Accelerators, Spectrometers, Detectors and Associated Equipment (2020) 163939.

[30] T. Rider, S. Calvard, Picture thresholding using an iterative selection method, IEEE Transactions on Systems, Man and Cybernetics 8 (1978) 630–632.

[31] J. Schindelin, I. Arganda-Carreras, E. Frise, Fiji: an open-source platform for biological-image analysis 9 (2012) 676–682.

[32] R. Beare, G. Lehmann, The watershed transform in itk-discussion and new developments. (2006). URL https://hal.inrae.fr/hal-02666802

[33] F. Toulemonde, F. Le Maou, Protection des éprouvettes de béton vis-à-vis de la dessiccation. le point sur quelques techniques de laboratoire, Bulletin de Liaison des Laboratoires des Ponts et Chaussées 203 (1996) 105–119.

[34] M. Boucher, Analyse du transfert spatio-temporel des déformations entre le coeur d'un ouvrage épais et son parement : application aux enceintes de confinement., Ph.D. thesis, Univ. Grenoble Alpes. France. (2016).

[35] E. Stavropoulou, E. Andò, A. Tengattini, M. Briffaut, F. Dufour, D. Atkins, G. Armand, Liquid water uptake in unconfined callovo oxfordian clay-rock studied with neutron and x-ray imaging., Acta Geotechnica 14 (2019) 19–33.

[36] T. Rougelot, Etude multi-échelles des couplages hydriques, mécaniques et chimiques dans les matériaux cimentaires., Ph.D. thesis, Université des Sciences et Technologies de Lille (2008).

[37] S. Poyet, Experimental investigation of the effect of temperature on the first desorption isotherm of concrete, Cement and Concrete Research 39 (11) (2009) 1052 – 1059. doi:https://doi.org/10.1016/j.cemconres.2009.06.019.

[38] S. Poyet, S. Charles, Temperature dependence of the sorption isotherms of cement-based materials: Heat of sorption and clausius–clapeyron formula, Cement and Concrete Research 39 (11) (2009) 1060–1067. doi:https://doi.org/10.1016/j.cemconres.2009.07.018.

[39] S. Dal Pont, S. Durand, B. Schrefler, A multiphase thermo-hydro-mechanical model for concrete at high temperatures—finite element implementation and validation under loca load, Nuclear Engineering and Design 237 (22) (2007) 2137 – 2150. doi:https://doi.org/10.1016/j.nucengdes.2007.03.047.

[40] D. Dauti, S. Dal Pont, M. Briffaut, B. Weber, Modeling of 3d moisture distribution in heated concrete: From continuum towards mesoscopic approach, International Journal of Heat and Mass Transfer 134 (2019) 1137 – 1152. doi:https://doi.org/10.1016/j.ijheatmasstransfer.2019.02.017.

[41] M. Thiery, V. Baroghel-Bouny, N. Bourneton, G. Villain, C. Stéfani., Modélisation du séchage des bétons - analyse des différents modes de transfert hydrique, Revue Européenne de Génie Civil (2007) 541–577.

[42] M. Van Genuchten, A closed-form equation for predicting the hydraulic conductivity of unsaturated soils., Soil Science Society of America Journal.

[43] J. Ožbolt, F. Oršanić, G. Balabanić, Modeling influence of hysteretic moisture behavior on distribution of chlorides in concrete, Cement and Concrete Composites 67 (2016) 73 – 84. doi:https://doi.org/10.1016/j.cemconcomp.2016.01.004.

[44] J. Zhang, J. Wang, Y. Han, Simulation of moisture field of concrete with pre-soaked lightweight aggregate addition, Construction and Building Materials 96 (2015) 599 – 614. doi:https://doi.org/10.1016/j.conbuildmat.2015.08.058.

[45] F. Soleilhet, F. Benboudjema, X. Jourdain, F. Gatuingt, Role of pore pressure on cracking and mechanical performance of concrete subjected to drying, Cement and Concrete Composites (2020) 103727doi:10.1016/j.cemconcomp.2020.103727.